Materials & Design 249 (2025) 113556

Contents lists available at ScienceDirect

Materials & Design

journal homepage: www.elsevier.com/locate/matdes

Excellent strength/ductility synergy by optimization of post-weld heat treatment for gas metal arc welded CoCrFeMnNi high entropy alloys with 410 stainless filler wire: High-throughput thermodynamic modelling with experimental validation

Jiajia Shen [a,b,*], Rae Eon Kim [c], Jingjing He [d], Jin Yang [e], J.G. Lopes [a], Zhi Zeng [f], N. Schell [g], Hyoung Seop Kim [c,h], J.P. Oliveira [a,b,*]

[a] UNIDEMI, Department of Mechanical and Industrial Engineering, NOVA School of Science and Technology, Universidade NOVA de Lisboa, 2829-516 Caparica, Portugal
[b] CENIMAT/I3N, Department of Materials Science, NOVA School of Science and Technology, Universidade NOVA de Lisboa, 2829-516 Caparica, Portugal
[c] Graduate Institute of Ferrous Technology, POSTECH (Pohang University of Science and Technology), Pohang 37673, South Korea
[d] Advanced Manufacturing Center, Ningbo Institute of Technology, Beihang University, Ningbo 315800, China
[e] School of Materials Engineering, Shanghai University of Engineering Science, Shanghai 201620, China
[f] School of Mechanical and Electrical Engineering, University of Electronic Science and Technology of China, Sichuan 611731, China
[g] Institute of Materials Physics, Helmholtz-Zentrum Hereon, Max-Planck-Str. 1, Geesthacht D-21502, Germany
[h] Advanced Institute for Materials Research (WPI-AIMR), Tohoku University, Sendai 980-8577, Japan

ARTICLE INFO

Keywords:
CoCrFeMnNi high entropy alloy
Welding
Thermodynamic calculation
Synchrotron X-ray diffraction
Mechanical properties testing

ABSTRACT

Post-weld annealing is a promising method for enhancing the performance of welded joints. However, traditional trial-and-error approaches are often time-consuming and inefficient, limiting their application in industrial production. To overcome this challenge, this study integrates high-throughput thermodynamic simulation techniques with a custom Python script to rapidly screen annealing temperatures for GMAWed CoCrFeMnNi high entropy alloy welded joints with ERNiMo-410 filler wire. By employing a combination of microstructural characterizations (such as Electron Backscatter Diffraction (EBSD) and Synchrotron X-ray Diffraction (SXRD)) and mechanical testing (including hardness testing and tensile Digital Image Correlation (DIC) analysis), the study validates the effects of selected annealing temperatures on the microstructure evolution and mechanical behavior of the welded joints. The results demonstrate that the optimized annealing temperature significantly enhances the uniformity of the microstructure and increases elongation at fracture by approximately sevenfold to 43.1 %, while maintaining comparable yield and ultimate strengths. This study highlights the potential industrial value of this method, offering an efficient and scientific approach for optimizing welded joint performance.

1. Introduction

In recent years, the equiatomic CoCrFeMnNi high entropy alloy (HEA) stands out for its exceptional mechanical properties across a wide temperature range [1]. However, translating these remarkable properties into practical applications hinges crucially on understanding and improving their weldability.

Extensive research has confirmed the excellent weldability of CoCrFeMnNi HEAs in both homogeneous and heterogeneous welding processes, across a variety of fusion-based welding techniques (such as [2,3]) and solid-state welding techniques [4]. However, challenges persist, including residual stress [5], microstructural heterogeneity [2], and the precipitation of hard and brittle phases [6] which remain major bottlenecks for welding these materials, limiting their applications under extreme environmental conditions. For instance, previous studies of GMAWed CoCrFeMnNi joints using different filler wires such as 410 stainless steel [7], 308 stainless steel [8], or Monel 400 [9], have shown good synergy between strength and ductility. Yet, the solid-state phase

* Corresponding authors at: CENIMAT/I3N, Department of Materials Science, NOVA School of Science and Technology, Universidade NOVA de Lisboa, 2829-516 Caparica, Portugal.
E-mail addresses: j.shen@fct.unl.pt (J. Shen), jp.oliveira@fct.unl.pt (J.P. Oliveira).

https://doi.org/10.1016/j.matdes.2024.113556
Received 24 October 2024; Received in revised form 2 December 2024; Accepted 18 December 2024
Available online 19 December 2024

transformations induced by the weld thermal cycle, such as recrystallization, grain growth, and precipitation of hard and brittle phases, resulted in softening of the heat affected zone (HAZ), formation of coarse columnar grains in the fusion zone (FZ), and significant microstructural disparities at the HAZ/FZ boundary, notably in the grain size gradient. These factors collectively increase the risk of joint failure. Therefore, there is a need to effectively optimize the post-welded joint performance of these materials to address these challenges.

So far, only one study by Nam et al. [10] has explored the effects of post-weld heat treatment (PWHT) temperatures ranging from 800 to 1000 °C on CoCrFeMnNi laser welded joints. The study revealed that compared to as-welded joints, the elongation of post-weld joints significantly increased with increasing annealing temperature, albeit at the expense of strength. In addition, there are currently five reported studies [11–15] on the annealing of other welded HEA systems. For instance, Palguna et al. [11] utilized an empirical approach to select 1100 °C as the annealing temperature for $Al_{0.3}CoCrFeNi$ welded joints. Similarly, Yebaji et al. [13] employed a comparable method to anneal $(Fe_{50}Mn_{30}Co_{10}Cr_{10})_{99}C_1$ welded joints at 1000 °C. These studies demonstrate that annealing at these temperatures can enhance the mechanical properties of the welded joints to varying extents. However, the selection of annealing temperatures in most cases still heavily relies on traditional trial-and-error methods. While such approach can occasionally yield suitable annealing conditions, it can be inherently inefficient, costly, and challenging to control with precision. Moreover, the trial-and-error method lacks systematic theoretical guidance, often requiring laborious experimental iterations to identify optimal annealing parameters. This issue is particularly pronounced for dissimilar welded joints. The compositional and structural complexity of these joints, combined with the effects of dilution on their microstructure and properties, further complicates the selection of appropriate annealing temperatures. In these cases, traditional trial-and-error approaches are often inadequate, as variations in dilution can significantly alter the microstructure and mechanical properties of the welded joints, resulting in unpredictable annealing outcomes. To date, no studies have addressed the systematic selection of annealing temperatures for dissimilar welded joints under varying dilution ratios, highlighting a critical gap that needs to be addressed. To address this research gap, the present study evaluates the effect of PWHT on GMAWed CoCrFeMnNi HEA joints using 410 stainless steels filler wire.

Thereby, to avoid a trial-and-error methodology and refine the focus of potential PWHT conditions, this study initially commenced by developing high-throughput thermodynamic simulations using ThermoCalc coupled with in-house developed Python scripts. Subsequently, experiments were conducted at annealing temperatures identified through thermodynamic simulation to explore the correlation between annealing process parameters, microstructure evolution, and mechanical properties in welded joints. The highlight of this study lies not only in the successful optimization of the performance of CoCrFeMnNi HEA welded joints through the proposed annealing strategy, but also in assessing the reliability and limitations of high-throughput calculations based on the CALPHAD method for annealing temperature screening. This approach provides new insights for the practical application of HEAs while also offering valuable experimental evidence for the application of thermodynamic simulation techniques in the field of thermo-mechanical processing of HEAs.

2. Materials and experiments

2.1. Materials and high-throughput thermodynamic modelling

A previous study [7] has thoroughly detailed the raw materials and welding procedures used for these joints.

Prior to annealing, the phase transformation behavior of welded joints over the annealing temperature range of 600 and 1200 °C was predicted by a thermodynamic calculation based on the CALPHAD method in combination with a customized Python script. The input composition was a blending of CoCrFeMnNi BM and 410 stainless steel filler wire, with 1 % as dilution steps (with 100 steps in total). Based on these simulation results, an annealing scheme was selected, involving holding at 1150 °C for one hour followed by water quenching to preserve the phase structure developed during the high temperature annealing.

2.2. Microstructural characterization and mechanical testing

For microstructural characterization, samples were polished and etched using Keller's reagent. Electron Backscatter Diffraction (EBSD) was conducted to analyze the welded joint on a Helios JSM-7100F. Synchrotron X-ray diffraction (SXRD) was utilized to study the phase structure evolution of the joints after PWHT, at P07 beamline of DESY with a wavelength of 0.14235 Å, focusing particularly on the identification of precipitate phases. Although Transmission Electron Microscopy (TEM) has significant advantages in precipitate phase detection, synchrotron radiation was chosen as an alternative method in this study. Synchrotron radiation, with its unique advantages of high energy, high resolution, and strong penetration capability, makes it an ideal tool for analyzing microstructures. In this experiment, the synchrotron radiation source had an energy of 78.1 keV, corresponding to a wavelength of 0.14235 Å, enabling efficient analysis of complex microstructural features. Furthermore, Scanning Electron Microscopy with Energy-Dispersive X-ray Spectroscopy (SEM-EDS) was used as an auxiliary tool to enhance the capability of precipitate phase detection and analysis when combined with synchrotron radiation. For the evaluation of mechanical properties, microhardness testing was conducted using a Mitutoyo HM-112 hardness tester with a 500 N load, and uniaxial tensile testing was carried out at room temperature on a Shimadzu tensile machine equipped with a 50 kN load cell with a strain rate of 1×10^{-3} s^{-1}. Digital image correlation (DIC) was performed during tensile testing. Here, it is important to highlight that DIC, with its non-contact image capture and analysis, effectively avoids the potential interference associated with traditional contact-based devices such as clamps and extensometers during tensile testing. Besides, DIC technology can accurately track the mechanical response across any region of a welded joint, making it especially valuable for analyzing complex or hard-to-measure areas, such as the small FZ within welded joints. Furthermore, DIC technology eliminates the need to separate or cut different parts of the welded joint (such as the BM, HAZ, and FZ) from the intact structure. This avoids the stress release that can occur during cutting, preserving the original stress states of these areas. As a result, the measurements obtained through DIC are more representative of the mechanical behavior in real-world applications, ensuring greater authenticity and reliability.

3. Results and discussion

3.1. High-throughput thermodynamic modelling predictions

Fig. 1 depicts the evolution in phase structures in a GMAWed joint of CoCrFeMnNi HEA with 410 stainless steel filler wire, across various dilution ratios and annealing temperatures. This visualization was created and obtained by large scale thermodynamic calculations. On the X-axis, the dilution rate changes at 1 % intervals, representing a transition from pure 410 stainless steel filler wire (0 %) on the left, to pure CoCrFeMnNi HEA BM (100 %) on the right. Simultaneously, the Y-axis represents the annealing temperature, ranging from 600 to 1200 °C, in 50 °C increments. The chart employs numbers 1 through 6 to encode the number of phase structures expected to be formed under specific dilution rates and annealing temperatures. Each number correlates with the formation of 1 to 6 distinct phase structures.

By analyzing the thermodynamic-obtained data, it becomes evident that the number of phase structures formed exhibits a decreasing trend

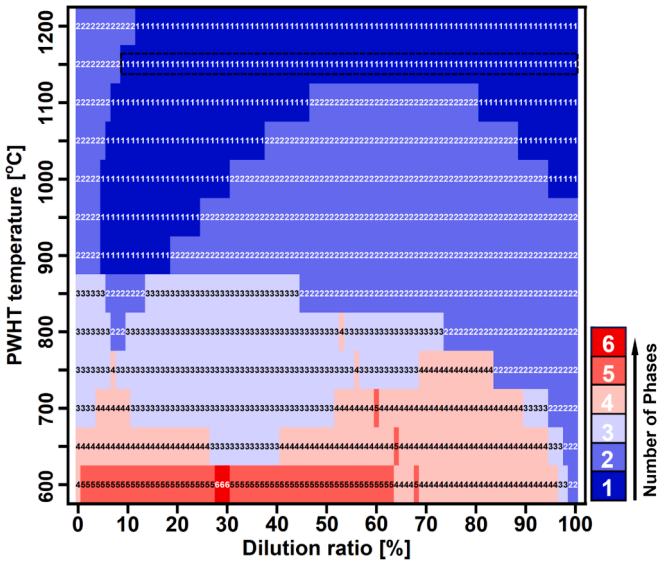

Fig. 1. Thermodynamic calculations as a function of the number of existing phases predicted for different dilutions and annealing temperatures. 0 % dilution corresponds to the ERNiMo-410 filler wire, while 100 % dilution corresponds to CoCrFeMnNi HEA BM.

with the gradual increase in annealing temperature. Particularly noteworthy is the prevalence of the single-phase FCC structure at an annealing temperature of 1150 °C, constituting up to 90 %, and widely distributed in the dilution range of 10–100 % (as indicated by the black dashed box in the Fig. 1). However, within the specific range of 0–9 % dilution, alongside the dominant FCC matrix phase, the presence of σ phase is also expected. According to previous research reports [6], σ phase could adversely affect the material's strength and ductility. Hence, maximizing the avoidance of brittle precipitate formation was established as the criterion for selecting the annealing temperature, with 1150 °C identified as the optimal annealing temperature. At this temperature, the material is expected to be composed of a single-phase FCC.

3.2. *Experimental validation: microstructural evolution*

To validate the effect of the selected PWHT condition on the microstructure of the welded joint, Fig. 2 presents the microstructural morphology of different regions from the annealed welded joint and the crystallographic features obtained through EBSD maps.

Upon examination of the macrostructure of the annealed welded joint (Fig. 2a)) alongside the optical micrographs of each respective region (Fig. 2b)), it can be observed that there is no significant difference in the microstructure between the BM and the HAZ, with both regions characterized by equiaxed grains harboring numerous annealing twins. Conversely, the FZ exhibits a coarse columnar grain structure. Notably, the PWHT significantly altered the grain size in various regions of the welded joint. Specifically, following annealing, the grain sizes of the BM, HAZ, and FZ increased from as-welded conditions of 2, 32.5, and 350 μm [7] to 138 μm, 138 μm, and 669 μm, respectively (Fig. 2c). These differences in grain growth effect primarily stem from varying driving forces present in different regions of the welded joint prior to annealing, which facilitate solid-state phase transformations, including pre-stored strain energy, dislocation density, and initial grain size. Especially, the coarse grain structure of the FZ. Current research indicates that the coarse grains in the FZ are primarily due to the high input during the welding process, as well as the high-temperature annealing treatment. Besides, this process is also influenced by element diffusion behaviour and the distribution of secondary phases at high temperatures. However, this study has not yet conducted an in-depth analysis of the high-temperature element diffusion behavior and the specific mechanisms of secondary phases in grain growth kinetics. Σ3 boundaries are generally formed during recrystallization. After annealing in both the BM and HAZ Σ3 boundaries are prevalent (Fig. 2d), which is attributed to the low stacking fault energy (SFE) of the CoCrFeMnNi HEA [16]. Notably, the proportion of Σ3 boundaries in these two regions is similar (≈41.2 % vs. ≈42.3 %, Fig. 2d), mainly because the formation of Σ3 boundaries in fully recrystallized grains is primarily determined by the final grain size (≈138 μm for both regions, see Fig. 2c). In the FZ, the content of Σ3 boundaries are relatively low (≈3.1 %), possibly due to the substantial consumption of Σ3 boundaries as nucleation sites during recrystallization. The entire welded joint after annealing exhibits low KAM values (≈0.57° (BM) vs. ≈0.55° (HAZ) vs. ≈0.57° (FZ), Fig. 2e), indicating that the observed recrystallization and grain growth effectively eliminate residual stress and decrease the dislocation density [17]. Finally, the grain structure in different regions of the welded joint after annealing does not show significant texture (Fig. 2f), with maximum pole densities of ≈2.74° (BM), ≈1.01° (HAZ), and ≈1.87° (FZ), mainly due to the increase in soaking time, smaller equiaxed grains continue to grow, thereby consuming textured grains.

Fig. 3a–c) shows representative X-ray diffraction patterns for BM, HAZ and FZ, respectively. From Fig. 3a) and b), it can be observed that after PWHT, both the BM and HAZ still predominantly consist of an FCC matrix phase with minor Cr-Mn oxide particles, consistent with previously observed pre-annealed structure [7]. Although the phase structure remained unchanged, the content of Cr-Mn oxides slightly increased after PWHT (BM: ≈1.7 % vs. ≈1.3 % [7], HAZ: ≈2.3 % vs. ≈1.8 % [7]), attributed to the high affinity of Cr and Mn elements with oxygen and enhanced diffusion of Mn and Cr during high temperature annealing. In contrast to the BM and HAZ, the FZ (Fig. 3c) after annealing contains not only an FCC matrix phase and Cr-Mn oxides (≈2.8 %) but also BCC (≈1.5 %), σ phase (≈0.8 %), and MnS phase (≈1.0 %). The formation of MnS phase during annealing is a newly identified phase structure, which is uncommon in previous studies. However, it aligns with findings from studies on stainless steel fabricated by selective laser melting (SLM) and subjected to heat treatment [18,19]. These studies demonstrated that MnS precipitates were absent prior to annealing and remained undetected detected in samples heat-treated at 900 °C or 1000 °C. However, their presence was clearly observed when the annealing temperature increased to 1100 °C or 1200 °C, highlighting the critical role of annealing temperature in promoting MnS precipitation. In the present study, the annealing temperature of 1150 °C falls within the range reported for MnS precipitates in the literature, making this observation plausible. Notably, MnS precipitates were not detected in the welded joint before annealing [7]. The underlying mechanism for MnS precipitates formation after high-temperature heat treatment remains unclear. One possible explanation is that the rapid cooling rate during the welding inhibits the sufficient interaction of Mn and S elements, preventing the immediate formation of MnS and leaving these elements dispersed in the matrix. During the subsequent annealing at 1150 °C, the system gradually approaches thermodynamic equilibrium, and the strong affinity between Mn and S [20,21] facilitates their interaction, leading to MnS precipitation. In future work, further investigations will focus on the transformation mechanism to achieve a deeper understanding of the behavior of MnS precipitates in welded joints during high-temperature annealing. Additionally, this study observed the presence of a Mn-Si-rich σ phase distinct from the Cr-rich σ phase detected before PWHT. The Cr-rich σ phase typically forms between 550 and 900 °C and disappears upon heat treatment above its equilibrium temperature [22]. In contrast, the Mn-Si-rich σ phase (≈0.8 %) observed here originates from the partial dissolution of BCC ferrite phase at high temperatures (BCC ferrite → σ phase transformation) [23]. Fig. 3d) and e) detail the distribution of Cr-Mn oxides, MnS phase, and Mn-Si-rich σ phase in the FZ through EDS mapping, further confirming the presence of these phases.

From the perspective of PWHT effects on phase structure formation, both the BM and the HAZ, corresponding to 100 % dilution condition

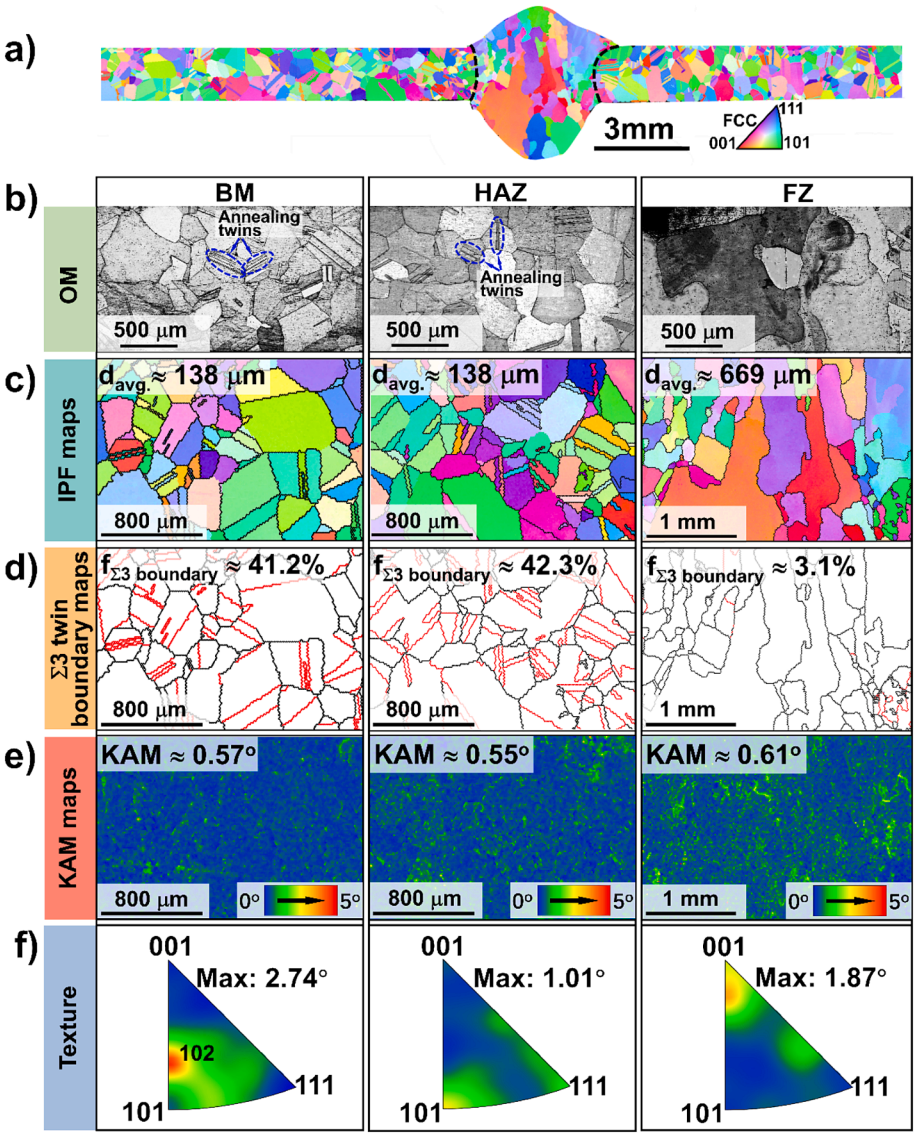

Fig. 2. Results of EBSD characterization. (a) EBSD map of the gas metal arc welded CoCrFeMnNi HEA with 410 stainless steel filler wire; (b)–(f) represent light optical microscopy, inverse pole figure (IPF), Σ3 boundaries, KAM and texture EBSD maps, respectively. From left to right: BM, HAZ, and FZ, respectively.

(Fig. 2), exhibit two phase structures after PWHT. The presence of Cr-Mn oxides in these regions is attributed to elemental contamination during the raw material preparation process [7]. This observation aligns with the phase structure predictions obtained from thermodynamic simulations that did not account for contamination (Fig. 2), suggesting a good accuracy of these simulations in predicting the phase structures in the BM and HAZ. However, in the FZ, the use of the selected PWHT revealed one matrix phase (FCC phase) and four precipitated phases (including Cr-Mn oxides, BCC, σ, and MnS phase). This significantly deviates from the phase structures predicted by thermodynamic calculations.

Several factors may contribute to these discrepancies between actual detection and thermodynamic predictions. Firstly, limitations in thermodynamic databases and models may not encompass all potential chemical systems and phase structures, especially in multicomponent alloy systems. Secondly, dynamic factors such as local concentrations of elements, diffusion rates, and grain growth rates play crucial roles in the actual formation of phase structures but are challenging to fully consider in simulations. Lastly, local microenvironments in the FZ before PWHT, such as temperature gradients and stress states, as well as compositional heterogeneity due to micro and macrosegregation as well as the development of Marangoni currents, may significantly influence the formation and evolution of phase structures, exceeding the capabilities of thermodynamic approach to effectively calculate the phase structure evolution. Future research efforts should focus on enhancing thermodynamic models and databases to better account for dynamic factors and the influence of local microenvironments, thereby improving the accuracy of simulation predictions.

3.3. Experimental validation: mechanical behavior

Fig. 4a) and b) depict the hardness mapping of the PWHT welded joint and a line scan obtained at middle height, respectively. From Fig. 4b), it can be observed that the hardness distribution of the welded joint after PWHT exhibits a concave shape. The BM and the HAZ have similar hardness values (≈118 HV0.5), which can be attributed to the fact that these two regions have the same grain size (≈138 μm, Fig. 2c)). The FZ has the lowest hardness value (≈90 HV0.5) due to the presence of coarse columnar grains (≈669 μm, Fig. 2c)). Although multiple precipitate phases formed in the FZ after PWHT (Fig. 3c), their low volume fraction did not significantly enhance their strength. Overall, compared to the hardness distribution of the pre-annealed welded joint [7], the welded joint after PWHT exhibits significant softening but high

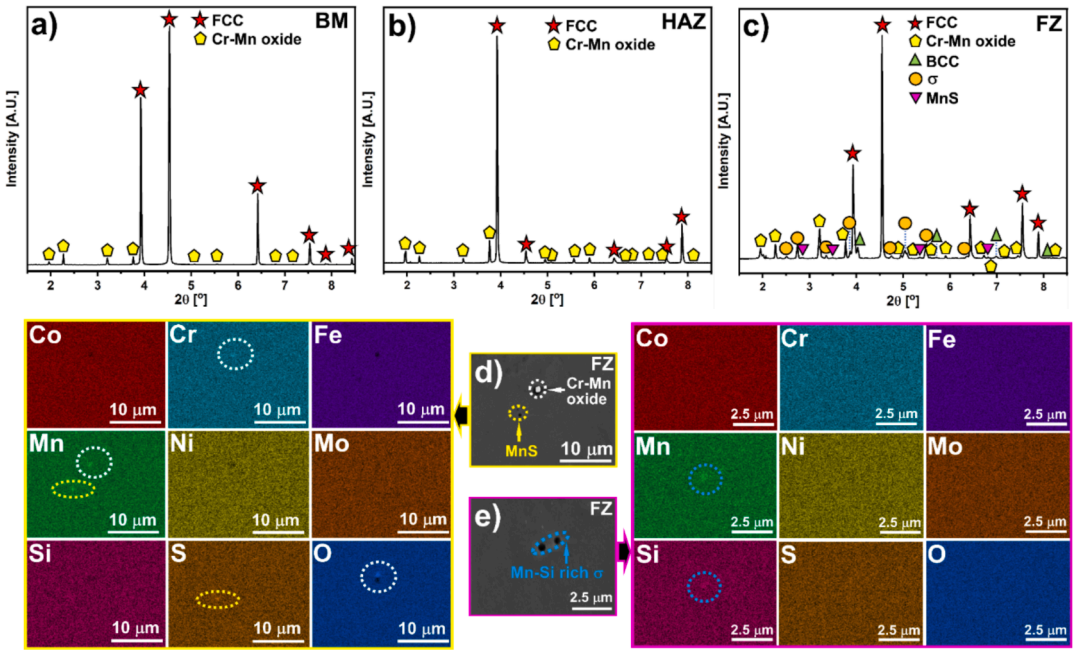

Fig. 3. Results of Synchrotron X-ray diffraction and EDS characterizations. (a)–(c) are representative diffraction patterns from the BM, HAZ, and FZ, respectively. (d) and (e) are SEM images and corresponding EDS mapping near particles of Cr-Mn oxide and MnS, as well as Mn-Si rich σ phase, respectively.

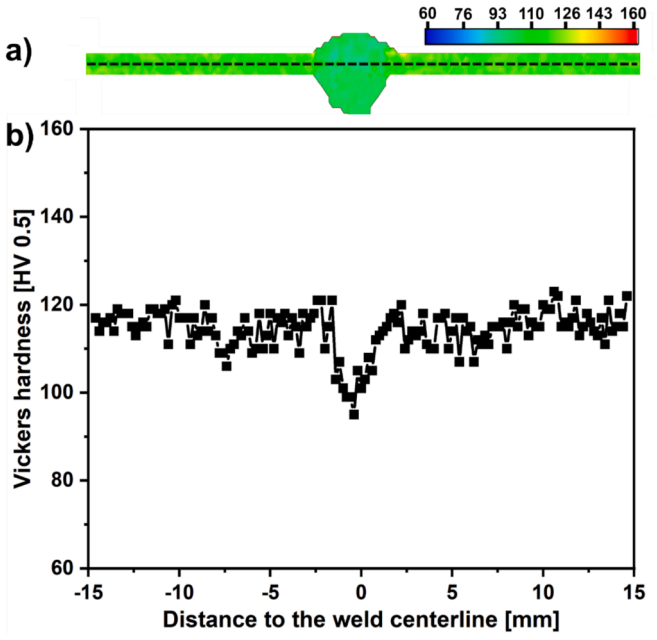

Fig. 4. Results of Vickers-hardness measurements. (a) Microhardness map of the whole welded joint; (b) Microhardness profile obtained along the middle height of the joint (black dashed line in (a)).

homogeneity (peak hardness difference is <30 HV0.5), which is related to the similar grain structure characteristics across the joint, in clear opposition to what existed in the as-welded material.

In the current study, tensile curves are obtained using two different methods: one is the tensile stress–strain curve from the tensile testing machine (refer to Fig. 5a)), which captures the overall mechanical behavior of the entire welded joint; the other is the tensile curve derived from DIC image analysis (refer to Fig. 5b)), which focuses on the local response of specific regions within the welded joint. During the loading process, different regions undergo deformation in distinct sequences, and certain local areas may preferentially deform at specific stages. As a result, the mechanical behavior varies across regions. This is why DIC technology provides more detailed local stress–strain data, helping to reveal how regional variations influence the overall mechanical performance. The detailed discussion is as follows. For mechanical behavior analysis, as shown in Fig. 5, the maximum strength and elongation of the annealed joint are approximately ≈587 MPa and ≈43.1 %, respectively. Compared to the pre-annealed condition, the elongation increased by approximately 7 times (≈43.1 % vs. ≈6.4 %), without a significant sacrifice in yield strength (≈242 vs. ≈313 MPa) and ultimate strength (≈587 vs. ≈641 MPa), the summary of tensile properties as shown in Fig. 5d). This enhancement is mainly attributed to the homogenization of the microstructure induced by the PWHT (Fig. 5). Although grain coarsening generally reduces material strength (according to the Hall-Petch effect), for the welded joints, the uniformity of the microstructure in different regions is more beneficial for improving its overall mechanical properties.

Furthermore, the fracture location shifted from the weld toe before PWHT [7] to the BM region after PWHT (Fig. 5a), further proving that the multiple precipitated phases formed in the FZ did not act as stress concentrators, thereby not adversely affecting the joint tensile mechanical. By combining the DIC strain maps (Fig. 5a) and the stress–-strain curves of different regions (Fig. 5b), it can be observed that during the entire tensile process, the deformation amount of the FZ is minimal. This is due to the larger effective cross-sectional area of the FZ, which means that under the same external tensile load, the force per unit area is smaller. Here, it is worth noting that the main steps for obtaining localized stress–strain curves from DIC data for the three typical regions include the following aspects: first, video conversion and image acquisition; second, post-processing of the captured images using the Ncorr MATLAB software; next, selecting a reference point and tracking its displacement trajectory; then, matching the load with the images; and finally, generating the stress–strain curves based on the above steps. Additionally, when the strain is less than ≈38.5 %, there is a significant stress concentration at the interface between the HAZ and the FZ. However, when the strain exceeds this threshold, the stress concentration area gradually shifts to the BM region. Considering that the BM region and the HAZ have similar microstructural characteristics (Fig. 2),

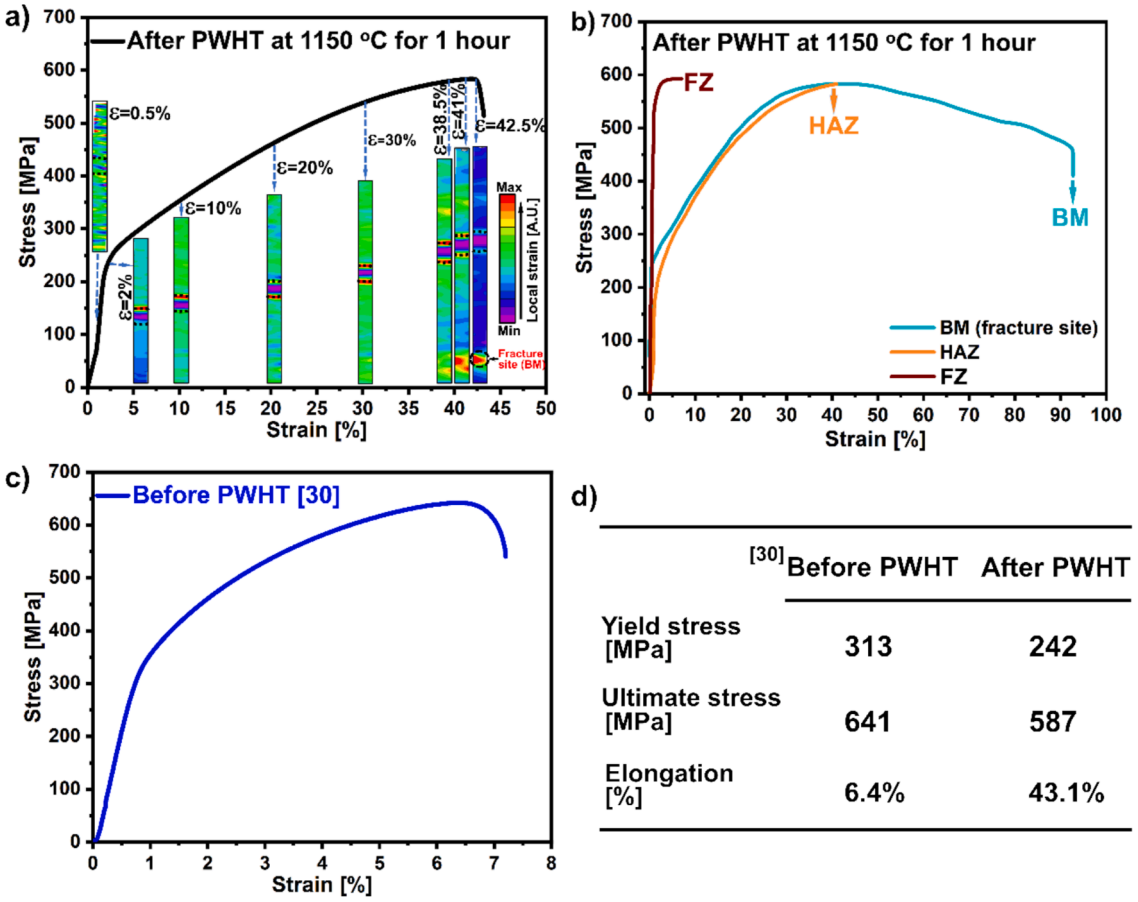

	[30] Before PWHT	After PWHT
Yield stress [MPa]	313	242
Ultimate stress [MPa]	641	587
Elongation [%]	6.4%	43.1%

Fig. 5. Results of tensile testing with DIC. (a) Engineering stress–strain curve of the GMAWed CoCrFeMnNi joints with ERNiMo-410 stainless steel filler wire after PWHT at 1150 °C for 1 h, with DIC snapshots captured at various strain levels during loading until failure, (b) Tensile curves derived from the DIC measurements for different regions across the joint: BM, HAZ, and FZ. (c) Engineering stress–strain curve of the GMAWed CoCrFeMnNi joints with ERNiMo-410 stainless steel filler wire before PWHT; (d) Summary of tensile properties of GMAWed CoCrFeMnNi joints with ERNiMo-410 stainless steel filler wire before and after PWHT.

it can be inferred that the fracture occurring in the BM region is likely due to the stress concentration caused by potential minor internal defects formed during the rolling process of the original BM. Here, it is important to emphasize that the breakthrough of this work lies not only in optimizing the GTAWed CoCrFeMnNi joints with ERNiMo-410 stainless steel filler wire through PWHT but also in the application and validation of high-throughput thermodynamic calculations for screening annealing temperatures. This approach demonstrates the tremendous potential and broad application prospects of high-throughput computation in optimizing material heat treatment processes. In future research, we will conduct a series of PWHT experiments at various annealing temperatures (e.g., 1000 °C and 1100 °C) to further investigate the specific effects of annealing temperature on joint performance.

In conclusion, the PWHT treatment optimized microstructural uniformity, significantly reduced residual stress, and improved strain distribution across the joint, thereby contributing to the observed strength-ductility balance. While grain growth can reduce strength, the combined effects of microstructural homogenization and residual stress release effectively compensated for this, resulting in a remarkable elongation increase (from ≈6.4 % to ≈43.1 %) with only a marginal decrease in ultimate tensile strength (from ≈641 MPa to ≈587 MPa). DIC analysis further revealed that stress concentration shifted to the BM region, reflecting improved deformation coordination and a reduced fracture risk in the FZ. It is worth mentioning that the current study focused on utilizing ThermoCalc software, combined with an in-house developed Python script, to rapidly screen optimal annealing temperatures through high-throughput thermodynamic simulations, followed by experimental validation of the predicted annealing conditions. The existing microstructural analysis, DIC testing, and mechanical property evaluation have sufficiently elucidated the intrinsic mechanisms by which PWHT enhances joint ductility. Further experiments involving microstructural characterization under different strain conditions, while scientifically valuable, fall beyond the scope of this study. In the future work, we plan to systematically investigate microstructural changes under various strain conditions to deepen our understanding of the deformation mechanisms in PWHT-treated joints. These will complement the current findings and provide more comprehensive insights into the interplay between microstructure and mechanical properties.

4. Conclusions

In this study, an optimum PWHT temperature was predicted using thermodynamic high-throughput calculations for the first time, and experimental validation was conducted. The main conclusions as follows:

- The weld joints were heat treated at the selected annealing temperature (1150 °C for one hour), with the BM and HAZ primarily consisting of a matrix FCC phase and Cr-Mn oxides. In contrast, the FZ included a matrix FCC phase and four precipitate phases: Cr-Mn oxide, BCC, σ, and MnS phase.
- Despite the variety of precipitates formed in the annealed FZ, these precipitates did not adversely affect the mechanical properties of the joint.

- Comparing experimental findings with thermodynamic simulations revealed higher accuracy in predicting the phase structure of the BM and HAZ but significant discrepancies in predicting the FZ's phase structure, with the chemical complexity across the FZ aiding in this.
- The heat weld joints exhibited softening compared to the as-welded condition. Although grain coarsening reduces the joint strength to some extent, the microstructural homogeneity dominates and allow to obtain excellent strength/ductility synergy: the ductility of the joint was significantly improved (≈43.1 % vs. ≈6.4 %) without notoriously sacrificing strength (≈587MPa vs. ≈641 MPa).

CRediT authorship contribution statement

Jiajia Shen: Writing – review & editing, Writing – original draft, Visualization, Validation, Software, Resources, Project administration, Methodology, Investigation, Formal analysis, Data curation, Conceptualization. **Rae Eon Kim:** Software, Formal analysis, Data curation. **Jingjing He:** Validation, Funding acquisition. **Jin Yang:** Validation, Investigation, Funding acquisition. **J.G. Lopes:** Validation, Investigation. **Zhi Zeng:** Validation, Resources, Funding acquisition. **N. Schell:** Resources, Investigation. **Hyoung Seop Kim:** Writing – review & editing, Writing – original draft, Visualization, Validation, Supervision, Resources, Project administration, Investigation, Conceptualization. **J. P. Oliveira:** Writing – review & editing, Writing – original draft, Visualization, Validation, Supervision, Software, Resources, Project administration, Methodology, Investigation, Funding acquisition, Formal analysis, Conceptualization.

Declaration of competing interest

The authors declare that they have no known competing financial interests or personal relationships that could have appeared to influence the work reported in this paper.

Acknowledgments

JS and JPO acknowledge the financial support provided by Fundação para a Ciência e a Tecnologia (FCT – MCTES) under the projects UID/00667/2020 (UNIDEMI), LA/P/0037/2020, UIDP/50025/2020 and UIDB/50025/2020. JS acknowledge to the China Scholarship Council for funding their Ph.D. studies (CSC NO. 201808320394). This research was also supported by the National Research Foundation of Korea (NRF), funded by the Ministry of Science and ICT (MSIP), through grant NRF-2021R1A2C3006662. The authors acknowledge DESY, a Helmholtz Association member in Hamburg, Germany, for providing experimental facilities and proposal I-20210899 EC. Additionally, this research was funded by the EU HORIZON 2020 Framework Program's CALIPSOplus project under Grant Agreement 730872. The study was supported by the International Cooperation Project of Ningbo City, No. 2023H018. The support is gratefully acknowledged.

Data availability

The code can be publicly provided based on user requests, but it cannot be used for commercial purposes.

References

[1] S.A. Krishna, N. Noble, N. Radhika, B. Saleh, A comprehensive review on advances in high entropy alloys: fabrication and surface modification methods, properties, applications, and future prospects, J. Manuf. Process. 109 (2024) 583–606, https://doi.org/10.1016/j.jmapro.2023.12.039.

[2] P. Zhang, Y. Qi, Q. Cheng, X. Sun, Welding dissimilar alloys of CoCrFeMnNi high-entropy alloy and 304 stainless steel using gas tungsten arc welding, J. Mater. Eng. Perform. 33 (2024) 3273–3282, https://doi.org/10.1007/s11665-023-08229-1.

[3] Z. Wu, S.A. David, D.N. Leonard, Z. Feng, H. Bei, Microstructures and mechanical properties of a welded CoCrFeMnNi high-entropy alloy, Sci. Technol. Weld. Join. 23 (2018) 585–595, https://doi.org/10.1080/13621718.2018.1430114.

[4] S. Park, H. Nam, J. Park, Y. Na, H. Kim, N. Kang, Superior-tensile property of CoCrFeMnNi alloys achieved using friction-stir welding for cryogenic applications, Mater. Sci. Eng. A 788 (2020) 139547, https://doi.org/10.1016/j.msea.2020.139547.

[5] W. Deng, D. Li, Y. Sang, Microstructure characterization and mechanical properties of electron beam welded joints of WRe alloy and CoCrFeNi high entropy alloys, Intermetallics 164 (2024) 108117, https://doi.org/10.1016/j.intermet.2023.108117.

[6] T.H. Kim, J. Jung, J.W. Bae, Suppressed plastic anisotropy via sigma-phase precipitation in CoCrFeMnNi high-entropy alloys, Materials (basel) 17 (2024) 1265, https://doi.org/10.3390/ma17061265.

[7] J. Shen, R. Gonçalves, Y.T. Choi, J.G. Lopes, J. Yang, N. Schell, H.S. Kim, J. P. Oliveira, Microstructure and mechanical properties of gas metal arc welded CoCrFeMnNi joints using a 410 stainless steel filler metal, Mater. Sci. Eng. A 857 (2022) 144025, https://doi.org/10.1016/j.msea.2022.144025.

[8] J. Shen, R. Gonçalves, Y.T. Choi, J.G. Lopes, J. Yang, N. Schell, H.S. Kim, J. P. Oliveira, Microstructure and mechanical properties of gas metal arc welded CoCrFeMnNi joints using a 308 stainless steel filler metal, Scr. Mater. 222 (2023) 115053, https://doi.org/10.1016/j.scriptamat.2022.115053.

[9] J. Shen, Y. Taek Choi, R. Gonçalves, N. Schell, J. Yang, Z. Zeng, A. Catarina Baptista, H. Seop Kim, J.P. Oliveira, Synergistic effects of Monel 400 filler wire in gas metal arc welding of CoCrFeMnNi high entropy alloy, Mater. Des. 242 (2024) 112996, https://doi.org/10.1016/j.matdes.2024.112996.

[10] H. Nam, C. Park, C. Kim, H. Kim, N. Kang, Effect of post weld heat treatment on weldability of high entropy alloy welds, Sci. Technol. Weld. Join. 23 (2018) 420–427, https://doi.org/10.1080/13621718.2017.1405564.

[11] Y. Palguna, K. Sairam, A.R. Kannan, N.S. Shanmugam, R. Korla, J.P. Oliveira, Effect of post weld heat treatment on the microstructure and mechanical properties of gas tungsten arc welded Al0.3CoCrFeNi high entropy alloy, Scr. Mater. 241 (2024) 115887, https://doi.org/10.1016/j.scriptamat.2023.115887.

[12] H. Moghanni, K. Dehghani, A. Shafiei, Effects of process parameters on microstructure and mechanical properties of Al0.5CoCrFeNi high entropy alloy thin sheets using pinless friction stir welding, J. Mater. Res. Technol. 16 (2022) 1069–1089, https://doi.org/10.1016/j.jmrt.2021.12.050.

[13] S. Yebaji, T. Sudeep Kumar, A. Verma, H. Natu, D.S. Gowtam, T. Shanmugasundaram, Effect of Post-welding treatment on corrosion behavior of laser and gas Tungsten arc-welded (Fe50Mn30Co10Cr10)99C1 interstitial high-entropy alloy, JOM 75 (2023) 5568–5580, https://doi.org/10.1007/s11837-023-06210-w.

[14] X. Wang, B. Huang, T. Li, Y. Wu, X. Hong, J. Zheng, Y. Zhu, Effect of heat treatment on microstructure and properties of CrMnFeCoNiMo high entropy alloy coating, J. Mater. Res. Technol. 29 (2024) 311–322, https://doi.org/10.1016/j.jmrt.2024.01.123.

[15] N.K. Adomako, G. Shin, N. Park, K. Park, J.H. Kim, Laser dissimilar welding of CoCrFeMnNi-high entropy alloy and duplex stainless steel, J. Mater. Sci. Technol. 85 (2021) 95–105, https://doi.org/10.1016/j.jmst.2021.02.003.

[16] B.-R. Chen, A.-C. Yeh, J.-W. Yeh, Effect of one-step recrystallization on the grain boundary evolution of CoCrFeMnNi high entropy alloy and its subsystems, Sci. Rep. 6 (2016) 22306, https://doi.org/10.1038/srep22306.

[17] F. Otto, A. Dlouhý, C. Somsen, H. Bei, G. Eggeler, E.P. George, The influences of temperature and microstructure on the tensile properties of a CoCrFeMnNi high-entropy alloy, Acta Mater. 61 (2013) 5743–5755, https://doi.org/10.1016/j.actamat.2013.06.018.

[18] F. Andreatta, A. Lanzutti, R.I. Revilla, E. Vaglio, G. Totis, M. Sortino, I. de Graeve, L. Fedrizzi, Effect of thermal treatment on corrosion behavior of AISI 316L stainless steel manufactured by laser powder bed fusion, Materials (basel) 15 (2022) 6768, https://doi.org/10.3390/ma15196768.

[19] M. Laleh, A.E. Hughes, W. Xu, P. Cizek, M.Y. Tan, Unanticipated drastic decline in pitting corrosion resistance of additively manufactured 316L stainless steel after high-temperature post-processing, Corros. Sci. 165 (2020) 108412, https://doi.org/10.1016/j.corsci.2019.108412.

[20] R. Silva, D.J. Young, C.B.M. Junior, G.S. Vacchi, C.A.T. Alberto, A.M. de S. Malafaia, C. Pascal, C.A.D. Rovere, Role of cerium addition in enhancing the oxidation resistance of austenitic Fe-Mn-Si-Cr-Ni shape memory stainless steels at 800 °C: microstructure and oxidation mechanism, Corros. Sci. 209 (2022) 110788, https://doi.org/10.1016/j.corsci.2022.110788.

[21] D. Dias, S. Nakamatsu, C.A. Della Rovere, J. Otubo, N.A. Mariano, Characterization and corrosion resistance behavior of shape memory stainless steel developed by alternate routes, Metals (basel) 10 (2019) 13, https://doi.org/10.3390/met10010013.

[22] J.M. Costa, B.S. Monteiro, F.A. Rocha, M.S. Cunha, M.F. Vieira, E.W. Sequeiros, The heat treatment effects on the microstructure, hardness, and sigma phase content of L-PBF SAE 316L stainless steel, Acad. Mater. Sci. (2024) 1–10, https://doi.org/10.20935/AcadMatSci6230.

[23] A. Perron, C. Toffolon-Masclet, X. Ledoux, F. Buy, T. Guilbert, S. Urvoy, S. Bosonnet, B. Marini, F. Cortial, G. Texier, C. Harder, V. Vignal, P. Petit, J. Farré, E. Suzon, Understanding sigma-phase precipitation in a stabilized austenitic stainless steel (316Nb) through complementary CALPHAD-based and experimental investigations, Acta Mater. 79 (2014) 16–29, https://doi.org/10.1016/j.actamat.2014.06.066.